A distinctive patchy osteomalacia characterises *Phospho1*-deficient mice

Alan Boyde,[1] (iD) Katherine A. Staines,[2] Behzad Javaheri,[3] Jose Luis Millan,[4] Andrew A. Pitsillides[3] and Colin Farquharson[2]

[1]*Dental Physical Sciences, Barts and The London School of Medicine and Dentistry, Queen Mary University of London, London, UK*
[2]*Roslin Institute and R(D)SVS, The University of Edinburgh, Midlothian, UK*
[3]*Comparative Biomedical Sciences, Royal Veterinary College, London, UK*
[4]*Sanford Children's Health Research Center, Sanford Burnham Prebys Medical Discovery Institute, La Jolla, CA, USA*

Abstract

The phosphatase PHOSPHO1 is involved in the initiation of biomineralisation. Bones in *Phospho1* knockout (KO) mice show histological osteomalacia with frequent bowing of long bones and spontaneous fractures: they contain less mineral, with smaller mineral crystals. However, the consequences of *Phospho1* ablation on the microscale structure of bone are not yet fully elucidated. Tibias and femurs obtained from wild-type and *Phospho1* null (KO) mice (25–32 weeks old) were embedded in PMMA, cut and polished to produce near longitudinal sections. Block surfaces were studied using 20 kV backscattered-electron (BSE) imaging, and again after iodine staining to reveal non-mineralised matrix and cellular components. For 3D characterisation, we used X-ray micro-tomography. Bones opened with carbide milling tools to expose endosteal surfaces were macerated using an alkaline bacterial pronase enzyme detergent, 5% hydrogen peroxide and 7% sodium hypochlorite solutions to produce 3D surfaces for study with 3D BSE scanning electron microscopy (SEM). Extensive regions of both compact cortical and trabecular bone matrix in *Phospho1* KO mice contained no significant mineral and/or showed arrested mineralisation fronts, characterised by a failure in the fusion of the calcospherite-like, separately mineralising, individual micro-volumes within bone. Osteoclastic resorption of the uncalcified matrix in *Phospho1* KO mice was attenuated compared with surrounding normally mineralised bone. The extent and position of this aberrant biomineralisation varied considerably between animals, contralateral limbs and anatomical sites. The most frequent manifestation lay, however, in the nearly complete failure of mineralisation in the bone surrounding the numerous transverse blood vessel canals in the cortices. In conclusion, SEM disclosed defective mineralising fronts and extensive patchy osteomalacia, which has previously not been recognised. These data further confirm the role of this phosphatase in physiological skeletal mineralisation.

Key words: backscattered-electron imaging; biomineralisation; osteoid; osteomalacia; PHOSPHO1.

Introduction

Bone formation depends on an integration of events orchestrated by the capacity of osteoblasts to synthesise, secrete and mineralise bone's extracellular matrix (ECM). This cascade of events, which culminates in mineral deposition in collagen (biomineralisation), is critical to skeletal structure, integrity and function throughout life (Kawasaki et al. 2009).

PHOSPHO1, a member of the haloacid dehalogenase superfamily, is highly expressed in bone and contributes to bone mineralisation through its participation in the formation of the initial hydroxyapatite seed crystals (Houston et al. 1999, 2004; Stewart et al. 2003, 2006; Roberts et al. 2007).

Treatment of developing chick embryos with lansoprazole, a small molecule that inhibits PHOSPHO1, completely inhibited mineralisation of all long bones (Macrae et al. 2010). Furthermore, bones from *Phospho1* knockout (KO) mice accumulate mineral poorly, leading to less stiff and more ductile bones in young juvenile mice (Huesa et al. 2011; Carriero et al. 2014; Rodriguez-Florez et al. 2015). This more compliant bone is consistent with the relative protection of long bones from *Phospho1* KO mice against fracture during three-point bending (Huesa et al. 2011). Also, the greater deformability is also consistent with the multiple skeletal abnormalities described in *Phospho1* KO

mice, which include osteomalacia, bowing of long bones and sporadic spontaneous fractures exhibiting a predominantly greenstick presentation (Yadav et al. 2011). Interestingly, this greater bone deformability appears to resolve in adult mice where the degree of stiffness in the *Phospho1* KO bones was corrected upon attainment of skeletal maturity (Javaheri et al. 2015). It is therefore likely that the optimal actions of PHOSPHO1 are most pronounced during rapid and timely ECM mineralisation in the early development of the skeleton, and that this contribution can be effectively mimicked by alternative mechanisms in later life (Millan, 2013; Yadav et al. 2016).

Studies by Yadav et al. (2011) have examined whether overexpression of tissue non-specific alkaline phosphatase (TNAP) can effectively prevent the development of skeletal abnormalities in *Phospho1* KO mice. They found that TNAP overexpression offered no apparent protection against the deleterious bone phenotype that develops in *Phospho1* KO mice despite the correction of plasma pyrophosphate (PPi) levels – a potent inhibitor of ECM mineralisation (Meyer, 1984) – in these mice. This suggests that PHOSPHO1 and TNAP have non-redundant functional roles during skeletal mineralisation. This is emphasised by the deletion of a single allele of *Alpl* in the *Phospho1* null background, which was found to aggravate the skeletal phenotype of *Phospho1* KO mice, whereas there was a complete absence of skeletal mineralisation in embryonic mice with a double ablation of *Phospho1* and *Alpl* function (Yadav et al. 2011).

In spite of this growing awareness of the contribution made by PHOSPHO1 to biomineralisation, our knowledge is mainly limited to observations made at the whole bone level (macroscale) where valuable information on bone structure and biomechanical properties of *Phospho1* KO mice have been reported. In contrast, the importance of the contribution of PHOSPHO1 to bone mineralisation at the micron resolution scale has been less well addressed. The aim of this present study was therefore to perform a mainly scanning electron microscopic (SEM)-based analysis of *Phospho1* KO bones to further clarify the function of this intracellular/intravesicular phosphatase in biomineralisation.

Materials and methods

Animal model

Phospho1-R74X-null mutant (*Phospho1* KO) mice were generated by N-ethyl-N-nitrosourea mutagenesis (ENU) as described previously (Yadav et al. 2011). Mice were housed up to four per cage in polypropylene cages with wood chip and paper bedding, and provided standard mouse chow and water *ad libitum* throughout the study. Weaners up to 8 weeks of age were fed a standard rodent breeding diet and thereafter a standard rodent maintenance diet (Special Diet Services, South Witham, UK). All procedures complied with the UK Animals (Scientific Procedures) Act 1986, and were reviewed and approved by the ethics committee of The Roslin Institute, University of Edinburgh.

PMMA embedding

Tibias and femurs from C57BL6 wild-type (WT) and *Phospho1* KO male mice (25–32 weeks old) were fixed in formaldehyde for 48 h, dehydrated in ethanol; substituted with xylene; infiltrated in pure methyl methacrylate monomer; then with monomer catalysed with α-azo-iso-butyronitrile at room temperature until rubbery; then finally hardened at 37 °C. The PMMA blocks were cut and polished to produce near longitudinal sections.

Backscattered-electron (BSE) SEM imaging

Uncoated PMMA blocks were imaged using 20 kV BSE imaging at 50 Pa pressure in a Zeiss EVO MA10 SEM (Zeiss, Cambridge, UK) - (Fig. 1A). To determine whether there were obvious differences in the degree of mineralisation in bone in WT and *Phospho1* KO mice, matching fields were imaged at identical sample-to-detector distances in quick sequence under stable instrument-operating conditions.

BSE SEM imaging of triiodide-stained PMMA block surfaces

To further characterise the histology of WT and *Phospho1* KO bones, block surfaces were stained with ammonium triiodide to reveal non-mineralised matrix (such as osteoid) and cellular components before further BSE SEM (Boyde, 2012b; Figs 1B, 2A–D and 3A,B).

Maceration using Tergazyme™ and hydrogen peroxide

To remove the cells and superficial non-mineralised collagen, we opened 70% ethanol-fixed bones with carbide milling tools to expose the endosteal surfaces, which were then macerated with alkaline bacterial pronase (Tergazyme™, Alcanox, New York, NY, USA: Boyde, 2012a) at 50 °C and 5% H_2O_2 at room temperature. The samples were subsequently washed, dehydrated in ethanol and air-dried to produce uncoated surfaces for study with 3D 20 kV BSE SEM, again at ~50 Pa chamber pressure (Fig. 4A–E).

X-ray micro-tomography (XMT)

For additional 3D characterisation, we used XMT (1172 X-ray micro-tomograph, Skyscan, Belgium). Bones from male WT and *Phospho1* KO mice were fixed in 70% ethanol and stored until scanning, with X-ray tube operated at 50 kV and 200 μA 1600 ms exposure time with a 0.5-mm aluminium filter, voxel size 5 μm, 0.6° rotation angle, two frame averaging, of whole bones before embedding in PMMA. Trimmed PMMA blocks were scanned again after SEM imaging 3D, when rendering was performed using Drishti software (Australian National University, Canberra: Fig. 3C).

Preparation of 10 μm ground section from SEM block face

In one instance, a 10μm-thick ground section of a *Phospho1* KO block face studied by BSE SEM both before and after iodine staining and after XMT was prepared. The block face was glued to a 1-mm-thick glass slide with cyano-acrylate adhesive. A 1030-nm laser operated in pulsed mode to give tissue ablation was
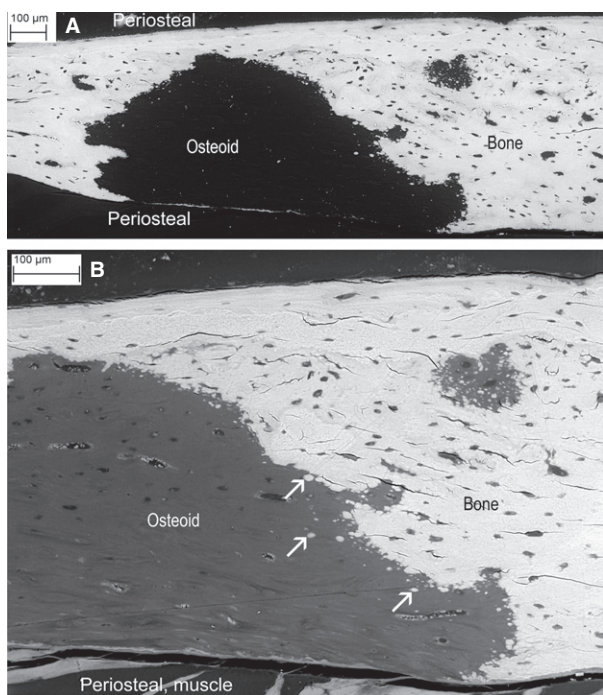
Fig. 1 (A) Backscattered-electron (BSE) of tibial cortex from Phospho1 knockout (KO) mouse showing one very large and several smaller patches of non-mineralised bone matrix, i.e. osteoid. Section plane is a tangent to the external surface. All scanning electron microscopy (SEM) images were recorded from uncoated samples, Zeiss EVO MA10 SEM, 20 kV, with 50 Pa chamber pressure to prevent electrostatic charging. (B) Part of the same region as (A) after ammonium triiodide staining to reveal non-mineralised matrix and cellular components. Arrows show patches of mineralised matrix within the background of non-mineralised matrix osteoid and along the arrested mineralising front.

used to cut the block at ~15 μm into the tissue ('TissueSurgeon', Rowiak LaserSolutions GmbH, Hannover, Germany), the surface then being finished by gentle polishing on 4000 grade silicon carbide polishing paper. The section was mounted using glycerine, studied by plane-polarised light microscopy (Fig. 3D), and further stained with MacNeal's tetrachrome (Fig. 3E: George T Gurr, London, UK) and acridine red (Fig. 3F: Gurr) for conventional transmitted light microscopy.

Further SEM studies

After initial rounds of SEM study, many samples were re-prepared and re-examined by SEM. Some samples that had been macerated with Tergazyme and H_2O_2 were further treated with 5% available chlorine sodium hypochlorite (bleach) solutions, a more rigorous and vigorous method of removing non-mineralised collagenous matrices (Fig. 5A–D).

In some cases the bone was first re-prepared to provide better exposure of endosteal surfaces where these had been partially obscured in the initial preparation round. PMMA block surfaces were etched with an acid gel (Icon-Etch, DMG, Hamburg, Germany) followed by removal of demineralised matrix with sodium hypochlorite solution to leave surface casts of PMMA embedded space (Fig. 6A,B). Some samples that had been macerated as above

were embedded in PMMA, and block faces polished as above (supplementary Fig. 6C,D in Appendix S1).

Results

Backscattered-electron imaging of PMMA block faces revealed extensive regions of compact, cortical bone matrix in *Phospho1* KO mice that contained no significant mineral and showed arrested mineralisation fronts. This arrest – not observed in any of the WT control bones studied – was demonstrated by the failure of fusion of the separately mineralising micro-volumes (Fig. 1A).

We therefore stained the samples with iodine or triiodide to reveal non-mineralised matrix and cellular components, which highlighted the distribution of non-mineralised matrix (osteoid). Elliptical patches of mineralised matrix were regularly seen within the regions of non-mineralised matrix close to the otherwise mineralised matrix of *Phospho1* KO mice (Figs 1B, 2A–C, 3A,B and 6A).

Attempts to explore whether this patchy, arrested mineralisation occurred reproducibly at specific anatomical locations demonstrated instead that the extent and position varied considerably between animals, contralateral limbs and anatomical sites. There was also great variation in the size of the non-mineralised matrix areas, which ranged from zones approximately 50 μm across that were centred around the blood vessel canals in the cortex, to the largest patches that extended to the millimetre scale (Figs 1A,B, 2A–C and 3A–F). The vascular channel-associated deficiency appears to be the most frequent manifestation of defective biomineralisation in the *Phospho1* KO mice (Fig. 2A,B). Neither was ever observed in WT bones (Fig. 2D).

In order to more precisely define the biomineralisation deficit, we selected locations from BSE SEM imaging of iodine-stained PMMA block surfaces that we could readily identify and thus examine at a range of scales, using several methodologies (Fig. 3). By XMT, we were unable to discriminate PMMA as such from PMMA-embedded uncalcified bone and cartilage, or tendon and ligament, or bone marrow space. The non-mineralised matrix regions in bone therefore appeared as 'empty' space (Fig. 3C, see also supplementary Fig. 7 and video in Appendix S1), but nevertheless allowed spatial equivalence to be registered in the images of the entire bone segment.

Polarised-light examination of a ground section of the bone block face prepared by dual photon laser ablation and at the boundary between non-mineralised cortex and mineralised bone in these *Phospho1* KO mice revealed clear continuity of lamellae from mineralised to non-mineralised regions (Fig. 3D).

Tetrachrome (blue-green in Fig. 3E) or acridine red (pale purple, Fig. 3F) staining of this patch of non-mineralised tissue was positive, and resembled the staining colour and intensity observed in non-mineralised regions of osteoid found at forming bone surfaces. It is noteworthy that
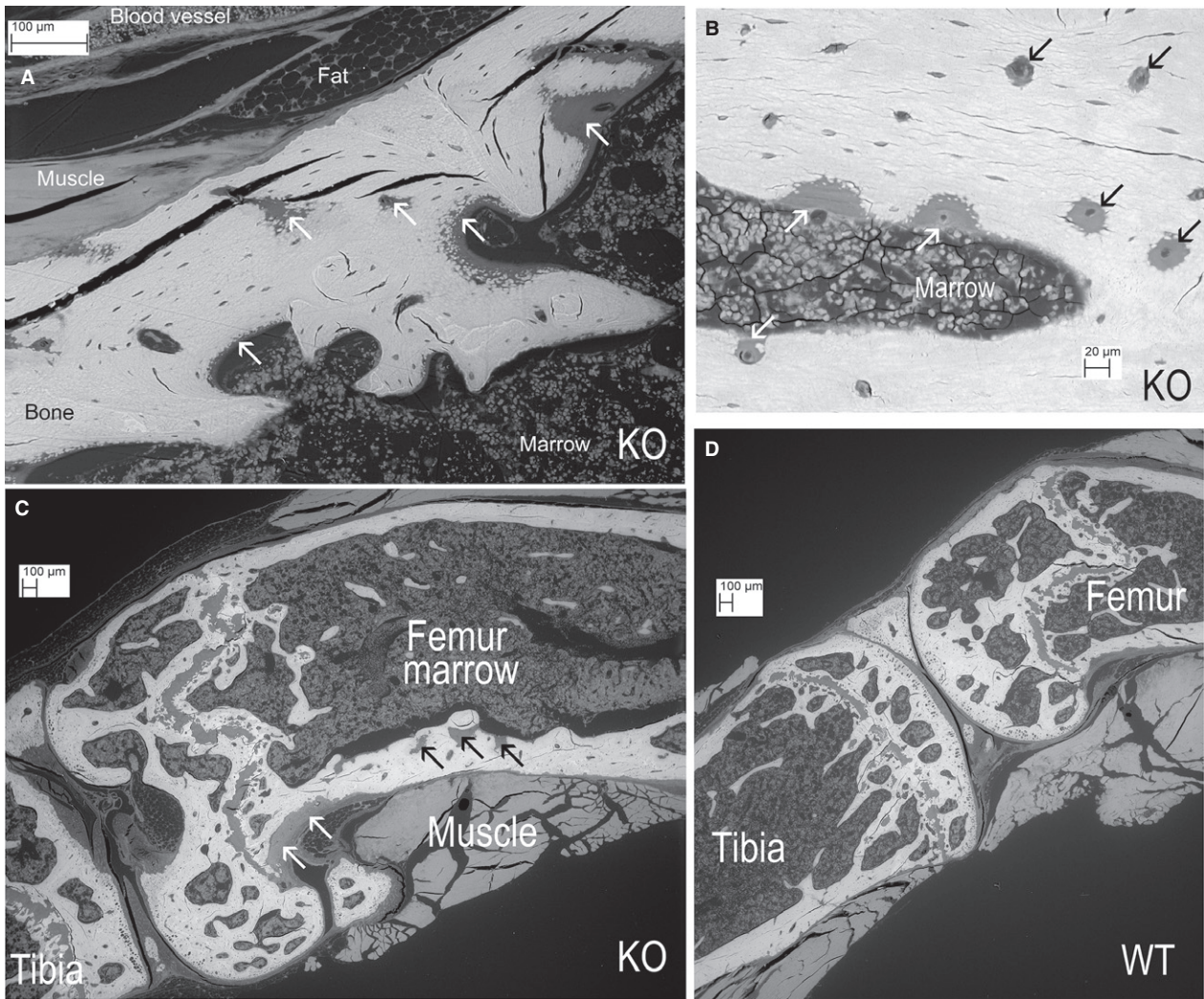
Fig. 2 (A) Knockout (KO). Proximal tibia showing many patches of mineralised matrix within areas of non-mineralised matrix osteoid (white arrows). (B) KO. Tibial diaphysis. White arrows show osteoid patches at endosteal, marrow surface. Black arrows show variation in the size of osteoid areas (down to zones 20–50 μm across) centred on the blood vessel canals in the cortex. (C) KO. Knee. Dense fibrous connective tissue of periosteum at white arrows, not to be confused with osteoid areas in cortex at black arrows. (D) Wild-type (WT) control knee, same scale.

osteocytes were present in the abnormal osteoid patches as seen both by iodine-stained SEM of block faces and light microscopy (Fig. 3B,E,F).

To visualise the calcified bone proper, we removed both cells and non-mineralised collagen with Tergazyme and H_2O_2 (Fig. 4). The mineralised matrices of the inorganic tissues were analysed following such 'maceration' by 3D BSE SEM morphological imaging (Boyde, 2012a). As some non-mineralised matrix osteoid remained after Tergazyme and H_2O_2 cleaning, we treated some samples additionally with sodium hypochlorite bleach (Fig. 5). This removed non-mineralised matrix remnants leaving a cleaner mineral front, making it easier to survey periosteal bone surfaces where fibrous periosteum, tendon or ligament residues are more difficult to remove.

Bones from *Phospho1* KO mice after Tergazyme and H_2O_2 cleaning exhibited extensive areas of osteoid and abnormal, arrested or defective mineralisation fronts on both the endosteal (Fig. 4A–D) and periosteal surfaces of the cortex and on trabeculae (supplementary Fig. 4G,H in Appendix S1). The WT control bones revealed endosteal surfaces with resorbed patches and fully mineralised (smooth) regions (Fig. 4E, supplementary Fig. 4F in Appendix S1).

The arrested or impeded collagen-fibre-bundle centred mineralisation in the *Phospho1* KO bones is indicative of osteomalacia. The observed hints of attenuation of osteoclastic resorption at the edges of uncalcified matrix patches in *Phospho1* KO bones (Figs 4D and 5A) is in line with the widely accepted understanding that osteoclasts hunt for mineral.
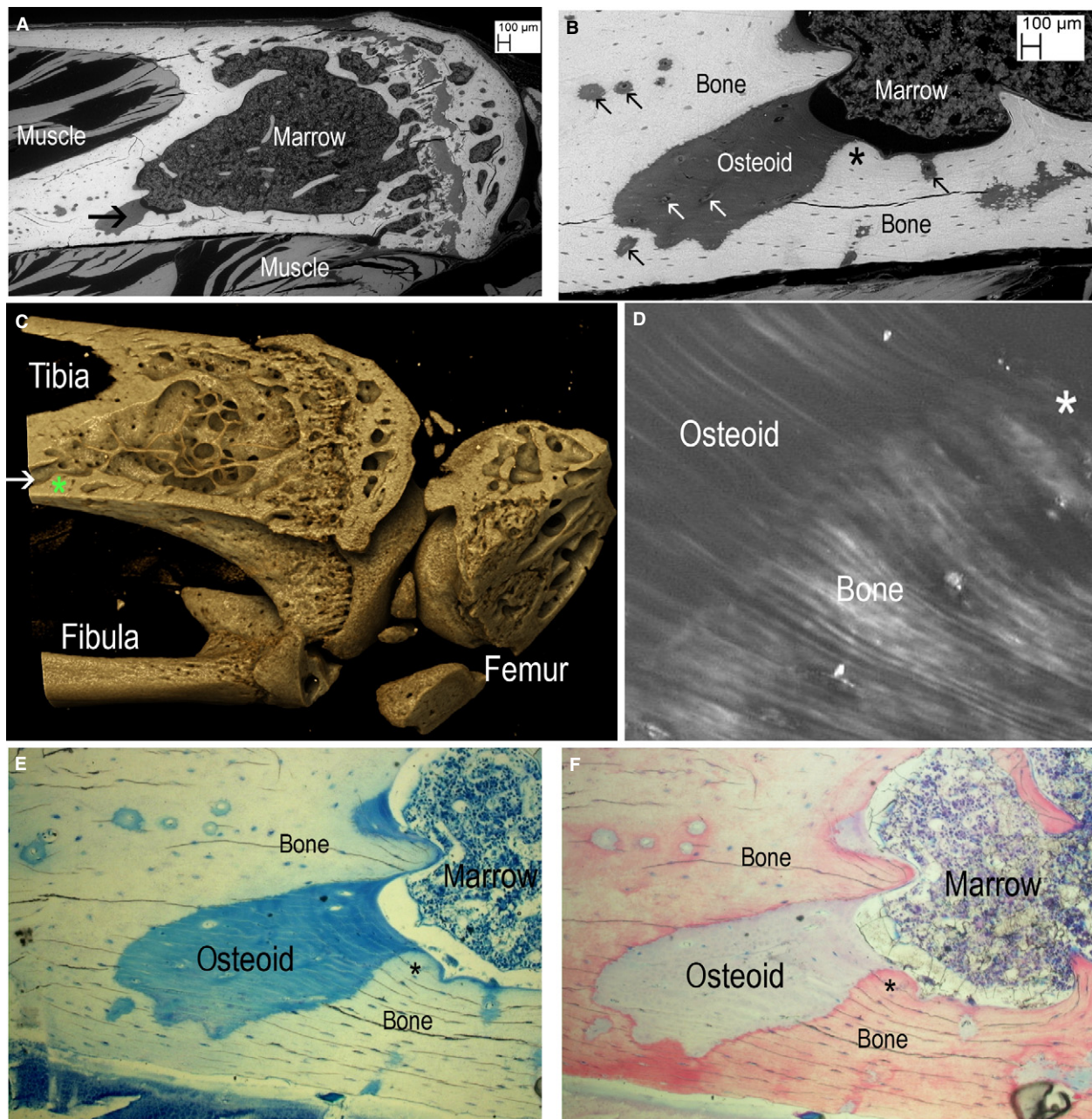
Fig. 3 (A–F) Correlation of block face backscattered-electron (BSE) scanning electron microscopy (SEM), X-ray micro-tomography (XMT) and polarised light microscopy (PLM) and ordinary light microscopy (LM). Asterix shows same spot in each part. (A) Knockout (KO) tibia. BSE SEM of ammonium triiodide-stained block face to reveal non-mineralised matrix osteoid and cellular components. Black arrow points to large osteoid patch. (After SEM studies we cut the blocks to make smaller samples for high-resolution XMT.) (B) Higher magnification view of large and small osteoid patches. Blood vessel canals are arrowed (black in bone and white in osteoid). Asterix shows spot similarly marked in (C–F). (C) Drishti reconstruction of XMT data. The large osteoid patch seen in (A and B) is shown as void (white horizontal arrow) in the rendered XMT image. This is in the same position as the black arrow in (A). (D) ~10-μm section of face of same block prepared by laser ablation (Rowiak 'TissueSurgeon') viewed between crossed polars, showing continuity between lamellae in mineralised bone and osteoid. Field width = 141 μm. (E) Same section, stained with Mac-Neal's tetrachrome stain giving green-blue tint to osteoid. Field width = 900 μm. (F) Same field stained with acridine red. Field width = 900 μm.

All macerated and bleached samples revealed very obvious areas of abnormal mineralisation fronts on trabecular bone, which can be clearly demarcated from regions of osteoclastic resorption (Fig. 5A, see also supplementary Fig. 6F,G in Appendix S1). This clear demarcation was also observed on endosteal surfaces (Fig. 5B), reinforcing the observation that aberrant mineralisation in Phospho1 KO mice attenuates resorption compared with surrounding
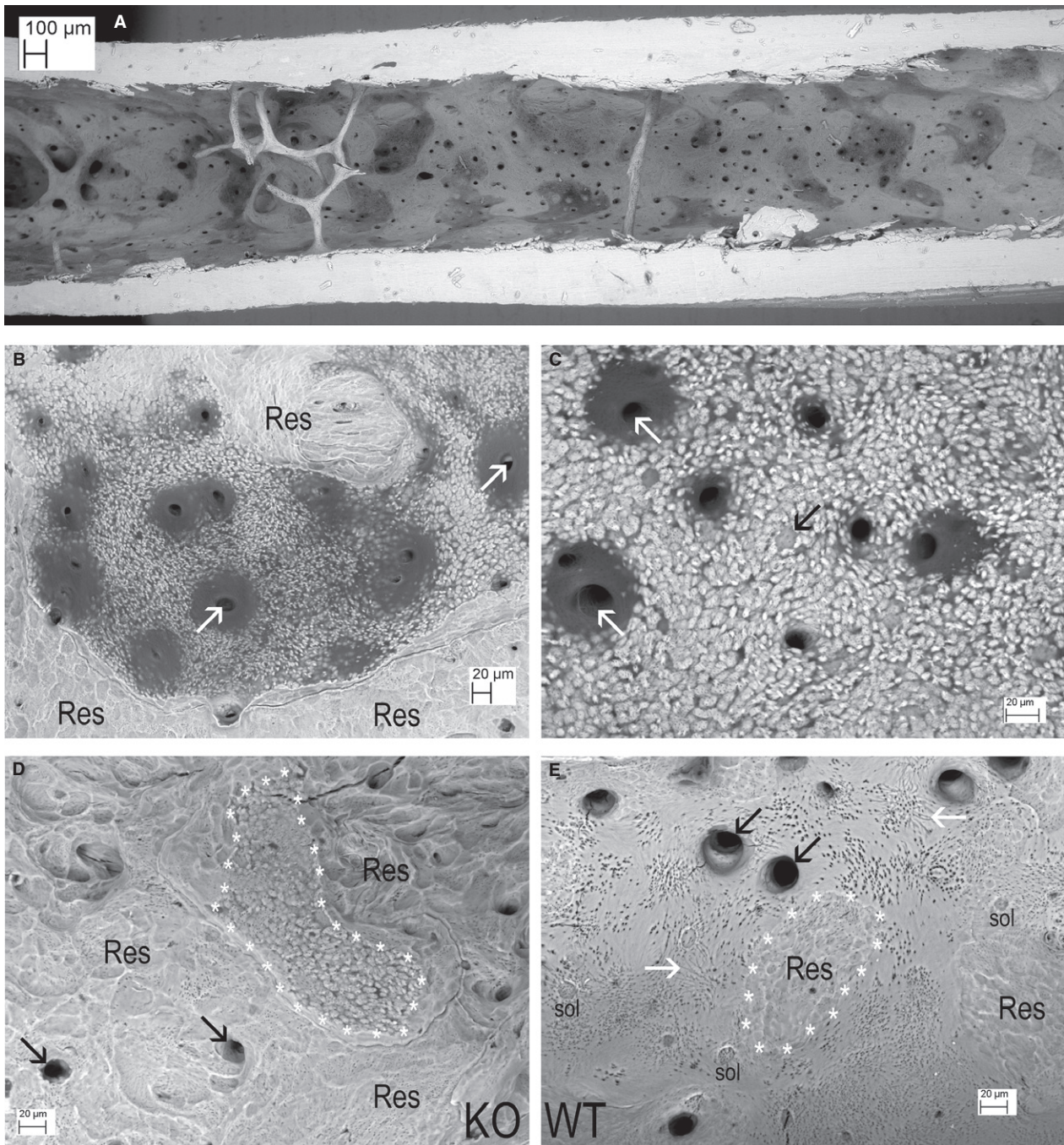
Fig. 4 (A) Central part of shaft endosteum in a Tergazyme macerated knockout (KO) femur. The dark patches are all abnormal osteoid [this scene is shown as a 3D anaglyph (red cyan) image in supplementary Fig. 4A in Appendix S1]. (B) Endosteum in a Tergazyme macerated KO tibia. Dark osteoid surrounds blood vessel canals (white arrows) within an area showing a mineralising front with unfused mineralising centres. This is surrounded by resorption (labels Res). (C) Endosteum in a Tergazyme macerated KO femur. Dark residual osteoid surrounds blood vessel canals (white arrows). Individual canaliculi show as small black dots (too small to label) within the unfused mineralising centres. The fully mineralised back wall of a forming osteocyte lacuna lies near dead centre of image at point of black arrow. (D) Endosteum in a Tergazyme and H$_2$O$_2$ macerated KO femur. The additional treatment removes residual osteoid from the endosteal surface and lining the blood vessel canals (black arrows). An area with abnormal mineralising front (outlined with white asterisks '*') is surrounded by resorption (Res). (E) Endosteum in a Tergazyme and hydrogen peroxide macerated wild-type (WT) tibia at the same scale, showing mostly a fully mineralised, smooth surface with some shallow resorbed patches (Res: one area outlined with white asterisks '*'). The openings of the blood vessel canals (black arrows) show a fully mineralised surface. Surface osteocyte lacunae above labels 'sol'. Some osteocyte lacunae are so superficial that their canaliculi lie in the plane of the fully mineralised (smooth) surface, showing as grey linear features in areas opposite points of white arrows. See also supplementary Fig. 4F in Appendix S1.
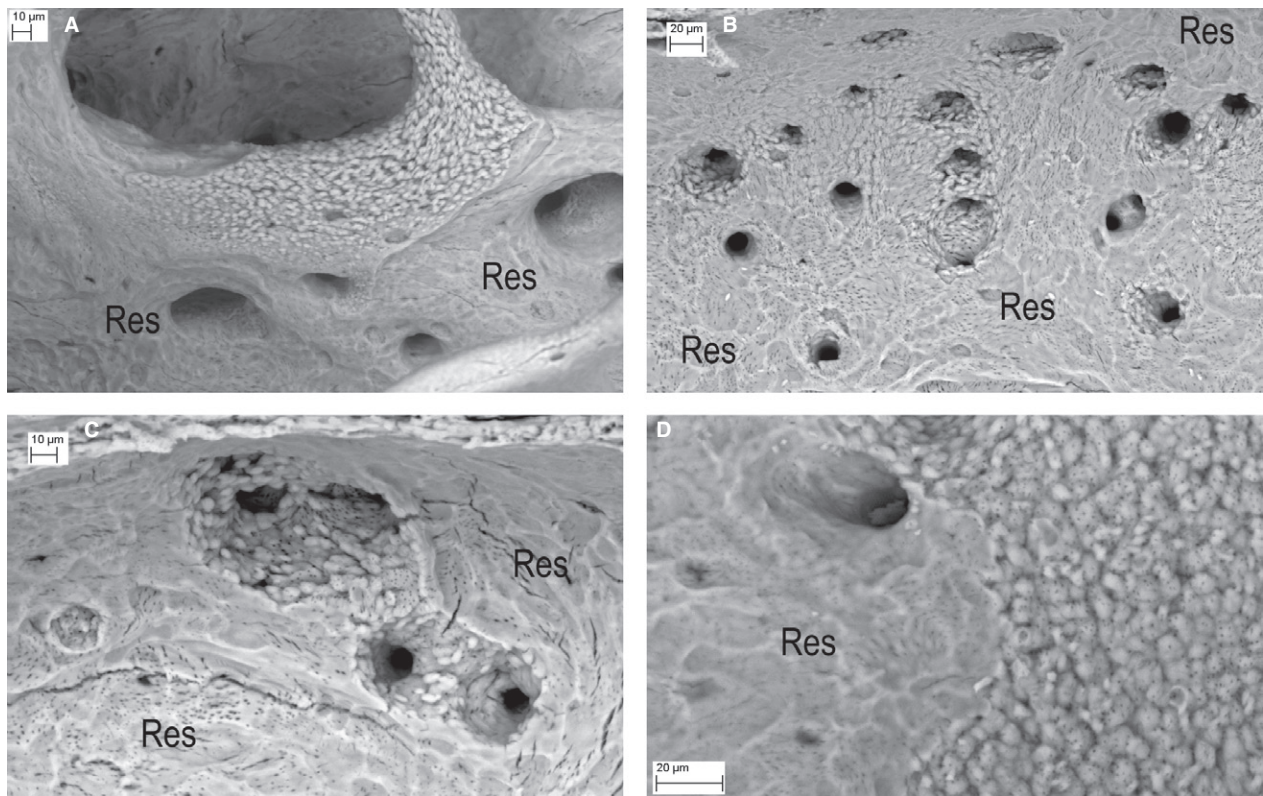
Fig. 5 Knockout (KO) endosteal surfaces after further cleaning with NaOCl bleach to remove all organic matrix, importantly here, any osteoid. (A) KO tibia. Osteoclastic resorption (Res) has not proceeded into the abnormal mineralisation front area on an endosteal trabecula. (B) KO tibia This is an area in which endosteal osteoclastic resorption (Res) has extended into bone with defective mineralisation surrounding blood vessel canal spaces (all the large dark features). There would have been osteoid everywhere that we see unfused mineralised patches. (C) KO tibia, cut edge at top. This is an area in which endosteal osteoclastic resorption (Res) has extended into an endosteal osteoid patch (now removed by NaOCl) analogous to the regions arrowed white in Fig. 2B. It again shows defective mineralisation surrounding blood vessel canal spaces (the large dark features). (D) KO femur. Unmineralised osteoid would certainly have been present over the right side of the field, which shows unfused mineralised regions in which canaliculi can be seen as small dark features. The left side had been subject to osteoclastic resorption (Res). Note that the mineralisation of this region – at the border – appears to be complete, i.e. the bone was uniformly mineralised where mineralised.

normally mineralised bone (Fig. 5A,B). This treatment also accentuated the failure of mineralisation in the bone, surrounding blood vessel canals in the cortices, where separately mineralised micro-volumes were very obvious. The individual, calcospherite-like micro-volumes could be seen to be multiply-penetrated by osteocyte canaliculi (Fig. 5C,D; see also supplementary Fig. 6C in Appendix S1).

Abnormal mineralising fronts were encountered much less frequently at periosteal surfaces, in keeping with the fact that it is the endosteal surfaces in both distal femur and proximal tibia that are largely formative, whilst periosteal surfaces show a higher incidence of resorbing or resting regions (Enlow, 1962).

Finally, we have used PMMA-embedded material that had subsequently been etched with acid and bleach to expose the non-mineralised regions as surface elevations and thus reveal the extent of the non-mineralised patches of bone in *Phospho1* KO mice in 3D. SEM studies of these etched PMMA blocks confirmed the extension of this non-mineralised bone into regions within the cortical bone of

these *Phospho1*KO mice and also provided scope to visualise the osteocyte content of both the non-mineralised patch of bone and the normally mineralised neighbouring cortices (Fig. 6A,B).

Discussion

Osteomalacia is often characterised by broad bands of osteoid with partial or complete failure of calcification, a phenotype that has been observed previously in *Phospho1* KO mice where the osteoid volume fraction is significantly increased (Yadav et al. 2011, 2014, 2016). The new data presented here suggest that the osteomalacia present in *Phospho1* deficiency may be locally more severe than previously reported, and yet be clearly delineated with an abrupt transition to normal tissue. Furthermore, previous studies of the endosteal surface of many genetically modified mice with defective bone mineralisation phenotypes had, as yet, never revealed the distinctive type of defective mineralisation observed in the *Phospho1* KO mice. This suggests to us that
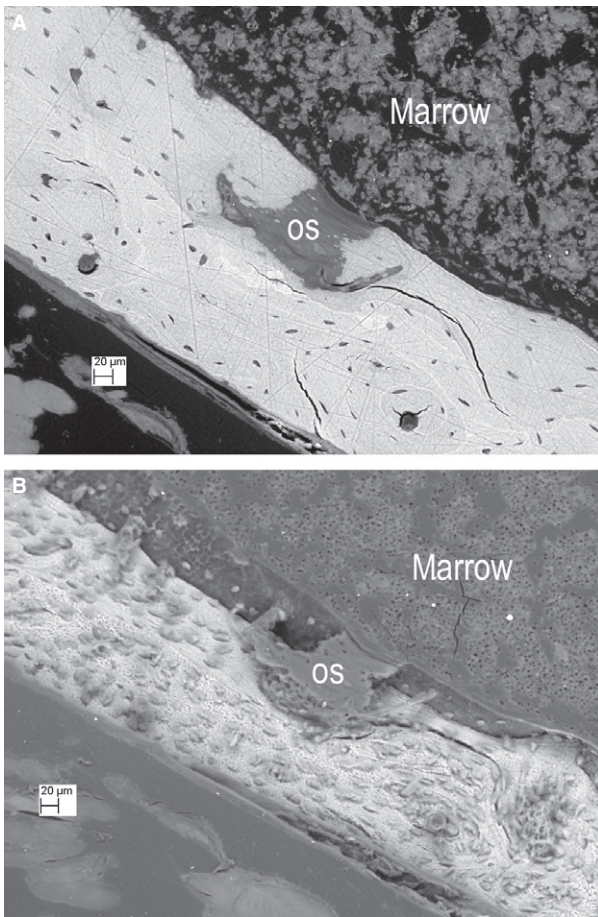
Fig. 6 Same field before and after etching. (A) Knockout (KO) tibia, PMMA-embedded ammonium triiodide stained to reveal soft tissue components, showing an osteoid patch at the centre. Surface normal to electron beam. [All other scanning electron microscopy (SEM) images in this MS were also recorded at normal electron beam incidence]. (B) The same region after 'DMG Icon-Etch' HCl gel etching for 1 min, followed by 5% NaOCl for 10 min and ammonium triiodide staining. PMMA within the osteoid patch (os) is left proud after the combined etch treatment. Osteocyte lacunae also appear as 'casts' above the etched surface. Surface tilted at 33 °.

the patchy osteomalacia noted in the *Phospho1* KO mice is not a general skeletal hallmark of hypomineralisation but is, as yet, rather a specific consequence of *Phospho1* deficiency.

The present observations were unexpected, and it is difficult to fully reconcile the presence of the stochastically distributed, relatively large patches of non-mineralised matrix with our present understanding of how PHOSPHO1 initiates the nucleation of bone mineral (Millan, 2013). Since the bone phenotype of *Phospho1* KO mice was first described, efforts have been focussed on elucidating the mechanisms by which PHOSPHO1 contributes to skeletal mineralisation. Systemic levels of calcium and phosphate are normal in *Phospho1* KO mice, and therefore the defect in bone mineralisation is likely to be at the cellular level (Yadav et al. 2011). A possible mechanism may involve the potent

calcification inhibitors, PPi, and osteopontin (OPN, encoded by the *Spp1* gene), whose plasma and bone expression levels are both elevated in *Phospho1* KO mice (Meyer, 1984; Speer et al. 2002; Steitz et al. 2002; Yadav et al. 2011, 2014). However, reducing the PPi levels in *Phospho1* KO mice by cross-breeding them to a transgenic strain expressing human TNAP under control of the ApoE promoter did not improve the skeletal phenotype of *Phospho1* KO mice (Yadav et al. 2011). In contrast, the development of the skeletal phenotype of *Phospho1* KO mice is prevented by the ablation of *Spp1* function and establishes a primary role for OPN, rather than PPi, in the aetiology of the osteomalacia observed in the *Phospho1* KO mice (Yadav et al. 2014).

Further efforts have centred on an early observation that PHOSPHO1 is present and active within matrix vesicles (MVs) where it may have a role in scavenging inorganic phosphate from MV membrane phospholipids (phosphocholine and phosphoethanolamine) to favour intra-vesicular hydroxyapatite deposition (Roberts et al. 2004; Stewart et al. 2006). Atomic force microscopy and Raman spectroscopy analyses have shown that chondrocyte-derived MVs from *Phospho1* KO mice have a decreased ability to initiate mineralisation (Yadav et al. 2016). These data extend our previous observations on mice KO in both *Phospho1* and *Alpl.* Although embryonic lethal, the embryos show a complete absence of skeletal mineralisation and MVs devoid of mineral (Yadav et al. 2011).

Immature woven bone, like peripheral or mantle dentine, normally contains large numbers of MVs, and the mineralisation pattern shows large numbers of small, separate micro-calcospherites (Boyde, 1980a,b, 2012a). The slowly formed lamellar bone in large bones in adult large mammals (including man) contains few, if any, MVs: the mineralisation process occurs instead by spreading through the collagen fibre bundles of the bone matrix giving rise to the very characteristic collagen-bundled centred mineralisation front pattern seen in anorganic (deproteinised) preparations for SEM (Boyde, 1980a,b, 2012a). On the other hand, the rapidly formed lamellar bone in small rodents shows a much larger number of separate centres, and it is much more difficult to visualise the collagen layout in the matrix in the mineralising 'front'. This would suggest that there are indeed large numbers of MVs. Then it becomes clear that MVs devoid of PHOSPHO1 will result in the observed mineralisation pattern demonstrated here, but why the distribution of this osteomalacia is patchy is unclear. One possible explanation is that PHOSPHO1 plays a much more subtle and pivotal role at the inception phase of mineralisation than previously considered. We propose that the mineralisation deficiency conferred by PHOSPHO1 deletion is initially insurmountable, mostly at certain locations, where rapid rates of mineralisation are otherwise unconstrained, and thus centred predominantly at endosteal and innermost perivascular surfaces. Long-term recovery from such patchy

osteomalacia in the more mature adult skeleton would therefore imply that this PHOSPHO1 function can eventually be overcome by potentially diverse, slower-acting mineralisation mechanisms.

Alternative proposed mechanisms for mineral nucleation include the precipitation and propagation of mineral crystals in the gap zone of collagen fibrils (Glimcher, 1987; Landis et al. 1993; Nudelman et al. 2010; Landis & Jacquet, 2013). Alternatively, electron microscopy and X-ray diffraction studies on human cortical bone have led others to propose that the majority of mineral is present outside of collagen fibrils and in the interfibrillar compartment, in the form of elongated mineral plate structures (McNally et al. 2012, 2013; Schwarcz et al. 2014). The results of ion beam thinning to prepare hard tissue sections for TEM have been interpreted as showing that mineral enwraps the collagen micro-fibril and is therefore within the fibril but topologically outside the (tropo)collagen molecules, the mineral phase being present as extremely long features unrelated to the gap zone (Boyde, 1974; Boyde & Pawley, 1976). This further explains why anorganic bone samples, such as those prepared by prolonged hypochlorite treatment, do not fall apart to make a suspension of fine crystals. Instead they permit us to study the mineralisation phenomena in 3D objects, as in several of the figures in this paper.

A novel concept that mineral may enter osteoid collagen as ready-packaged globules of disordered calcium phosphate (Mahamid et al. 2011; Kerschnitzki et al. 2016a,b) – perhaps with carbonate enrichment at initial mineral cluster sites (Nitiputri et al. 2016) – does not contribute to explaining the patchy nature of the histological osteomalacia, which is the focus of the present report.

PHOSPHO1 deficiency has been suggested to significantly increase osteocyte lacunae density and vascular content of cortical bone (Javaheri et al. 2015). These conclusions could, however, be explained by the present findings using higher resolution imaging as follows: the vascular canals are very frequently contained within the more numerous and smaller unmineralised matrix regions we reveal here. We show that osteoid cannot be distinguished from canal space by XMT, and the canals will therefore appear to be larger and to occupy a larger volume fraction. If there were, in addition, a thin seam of unmineralised matrix around some of the osteocyte lacunae – as is known to be the case in several instances of osteomalacia (Boyde, 1980a,b) – then the lacunae will be more effectively detected by XMT – the more so the better the resolution, and Javaheri et al. (2015) employed 0.6 μm – and the count will increase, as well as the volume fraction.

The 3D extent of the non-mineralised regions can be seen in XMT image sequences (supplementary Fig. 7 and video in Appendix S1). XMT resolution is inadequate in discriminating focal mineralisation defects from vascular/lacunar-canalicular changes, but XMT has the advantage of maintaining the sample whole. Co-registration of images from both modalities discloses very effective co-localisation of the areas of bone matrix devoid of mineral and highlights the relatively random targeting of osteomalacia in the cortical bone. The patchy dissemination of the most severe type of lesion is reminiscent of the mosaic distribution of lesions seen in fibrous dysplasia (Saggio et al. 2014). The present results with those shown earlier also disclose that osteocytogenesis seems to continue relatively unabated in the bones of *Phospho1* KO mice, including in the totally unmineralised osteoid regions, yet some cell culture and *in vivo* studies have previously suggested that ECM mineralisation is an essential regulator of osteocytogenesis (Irie et al. 2008; Prideaux et al. 2012). In conclusion, this study revealed the consequences of *Phospho1* deficiency on the microscale structure of mineralised bone. SEM disclosed defective mineralising fronts and extensive histological osteomalacia, which was most frequent in bone surrounding the numerous transverse blood vessel canals in the cortices. This extensive – but patchy or spotty – histological osteomalacia found in *Phospho1* KO lower limb bones has previously not been recognised. These data further confirm the necessity of this phosphatase for physiological mineralisation and the establishment of proper skeletal structure.

Acknowledgements

References

Boyde A (1974) Transmission electron microscopy of ion beam thinned dentine. *Cell Tissue Res* **152**, 543–550.

Boyde A (1980a) Electron microscopy of the mineralizing front. *Metab Bone Dis Relat Res* **2**, 69–78.

Boyde A (1980b) Evidence against osteocytic osteolysis. *Metab Bone Dis Relat Res* **2**, 239–255.

Boyde A (2012a) Scanning electron microscopy of bone. *Methods Mol Biol* **816**, 365–400.

Boyde A (2012b) Staining plastic blocks with triiodide to image cells and soft tissues in backscattered electron SEM of skeletal and dental tissues. *Eur Cell Mater* **24**, 154–161.

Boyde A, Pawley J (1976) Transmission electron microscopy of ion erosion thinned hard tissues. In: *Calcified Tissues (1975)*. (ed. Nielsen SP), pp. 117–123. Berlin: Springer.

Carriero A, Bruse JL, Oldknow KJ, et al. (2014) Reference point indentation is not indicative of whole mouse bone measures of stress intensity fracture toughness. *Bone* **69**, 174–179.

Enlow DH (1962) A study of the post-natal growth and remodeling of bone. *Am J Anat* **110**, 79–101.

Glimcher MJ (1987) The nature of the mineral component of bone and the mechanism of calcification. *Instr Course Lect* **36**, 49–69.

Houston B, Seawright E, Jefferies D, et al. (1999) Identification and cloning of a novel phosphatase expressed at high levels in differentiating growth plate chondrocytes. *Biochim Biophys Acta* **1448**, 500–506.

Houston B, Stewart AJ, Farquharson C (2004) PHOSPHO1-A novel phosphatase specifically expressed at sites of mineralisation in bone and cartilage. *Bone* **34**, 629–637.

Huesa C, Yadav MC, Finnila MA, et al. (2011) PHOSPHO1 is essential for mechanically competent mineralization and the avoidance of spontaneous fractures. *Bone* **48**, 1066–1074.

Irie K, Ejiri S, Sakakura Y, et al. (2008) Matrix mineralization as a trigger for osteocyte maturation. *J Histochem Cytochem* **56**, 561–567.

Javaheri B, Carriero A, Staines KA, et al. (2015) Phospho1 deficiency transiently modifies bone architecture yet produces consistent modification in osteocyte differentiation and vascular porosity with ageing. *Bone* **81**, 277–291.

Kawasaki K, Buchanan AV, Weiss KM (2009) Biomineralization in humans: making the hard choices in life. *Annu Rev Genet* **43**, 119–142.

Kerschnitzki M, Akiva A, Ben Shoham A, et al. (2016a) Bone mineralization pathways during the rapid growth of embryonic chicken long bones. *J Struct Biol* **195**, 82–92.

Kerschnitzki M, Akiva A, Ben Shoham A, et al. (2016b) Transport of membrane-bound mineral particles in blood vessels during chicken embryonic bone development. *Bone* **83**, 65–72.

Landis WJ, Jacquet R (2013) Association of calcium and phosphate ions with collagen in the mineralization of vertebrate tissues. *Calcif Tissue Int* **93**, 329–337.

Landis WJ, Song MJ, Leith A, et al. (1993) Mineral and organic matrix interaction in normally calcifying tendon visualized in three dimensions by high-voltage electron microscopic tomography and graphic image reconstruction. *J Struct Biol* **110**, 39–54.

Macrae VE, Davey MG, McTeir L, et al. (2010) Inhibition of PHOSPHO1 activity results in impaired skeletal mineralization during limb development of the chick. *Bone* **46**, 1146–1155.

Mahamid J, Addadi L, Weiner S (2011) Crystallization pathways in bone. *Cells Tissues Organs* **194**, 92–97.

McNally EA, Schwarcz HP, Botton GA, et al. (2012) A model for the ultrastructure of bone based on electron microscopy of ion-milled sections. *PLoS One* **7**, e29258.

McNally E, Nan F, Botton GA, et al. (2013) Scanning transmission electron microscopic tomography of cortical bone using Z-contrast imaging. *Micron* **49**, 46–53.

Meyer JL (1984) Can biological calcification occur in the presence of pyrophosphate? *Arch Biochem Biophys* **231**, 1–8.

Millan JL (2013) The role of phosphatases in the initiation of skeletal mineralization. *Calcif Tissue Int* **93**, 299–306.

Nitiputri K, Ramasse QM, Autefage H, et al. (2016) Nanoanalytical electron microscopy reveals a sequential mineralization process involving carbonate-containing amorphous precursors. *ACS Nano* **10**, 6826–6835.

Nudelman F, Pieterse K, George A, et al. (2010) The role of collagen in bone apatite formation in the presence of hydroxyapatite nucleation inhibitors. *Nat Mater* **9**, 1004–1009.

Prideaux M, Loveridge N, Pitsillides AA, et al. (2012) Extracellular matrix mineralization promotes E11/gp38 glycoprotein expression and drives osteocytic differentiation. *PLoS One* **7**, e36786.

Roberts SJ, Stewart AJ, Sadler PJ, et al. (2004) Human PHOSPHO1 exhibits high specific phosphoethanolamine and phosphocholine phosphatase activities. *Biochem J* **382**, 59–65.

Roberts S, Narisawa S, Harmey D, et al. (2007) Functional involvement of PHOSPHO1 in matrix vesicle-mediated skeletal mineralization. *J Bone Miner Res* **22**, 617–627.

Rodriguez-Florez N, Garcia-Tunon E, Mukadam Q, et al. (2015) An investigation of the mineral in ductile and brittle cortical mouse bone. *J Bone Miner Res* **30**, 786–795.

Saggio I, Remoli C, Spica E, et al. (2014) Constitutive expression of Gsalpha(R201C) in mice produces a heritable, direct replica of human fibrous dysplasia bone pathology and demonstrates its natural history. *J Bone Miner Res* **29**, 2357–2368.

Schwarcz HP, McNally EA, Botton GA (2014) Dark-field transmission electron microscopy of cortical bone reveals details of extrafibrillar crystals. *J Struct Biol* **188**, 240–248.

Speer MY, McKee MD, Guldberg RE, et al. (2002) Inactivation of the osteopontin gene enhances vascular calcification of matrix Gla protein-deficient mice: evidence for osteopontin as an inducible inhibitor of vascular calcification in vivo. *J Exp Med* **196**, 1047–1055.

Steitz SA, Speer MY, McKee MD, et al. (2002) Osteopontin inhibits mineral deposition and promotes regression of ectopic calcification. *Am J Pathol* **161**, 2035–2046.

Stewart AJ, Schmid R, Blindauer CA, et al. (2003) Comparative modelling of human PHOSPHO1 reveals a new group of phosphatases within the haloacid dehalogenase superfamily. *Protein Eng* **16**, 889–895.

Stewart AJ, Roberts SJ, Seawright E, et al. (2006) The presence of PHOSPHO1 in matrix vesicles and its developmental expression prior to skeletal mineralization. *Bone* **39**, 1000–1007.

Yadav MC, Simao AM, Narisawa S, et al. (2011) Loss of skeletal mineralization by the simultaneous ablation of PHOSPHO1 and alkaline phosphatase function: a unified model of the mechanisms of initiation of skeletal calcification. *J Bone Miner Res* **26**, 286–297.

Yadav MC, Huesa C, Narisawa S, et al. (2014) Ablation of osteopontin improves the skeletal phenotype of phospho1(-/-) mice. *J Bone Miner Res* **29**, 2369–2381.

Yadav MC, Bottini M, Cory E, et al. (2016) Skeletal mineralization deficits and impaired biogenesis and function of chondrocyte-derived matrix vesicles in Phospho1(-/-) and Phospho1/Pi t1 double-knockout mice. *J Bone Miner Res* **31**, 1275–1286.

Supporting Information

Additional Supporting Information may be found in the online version of this article:

Fig. 4A. anaglyph version for viewing with red (left eye) and cyan (right eye) spectacles on a computer/monitor screen. Central part of shaft endosteum in a Tergazyme macerated KO femur. The dark patches are all abnormal osteoid with unfused mineralising centres

Figure S4F. Tergazyme and hydrogen peroxide macerated WT femur showing endosteal surface with resorbed patches (Res) and fully mineralised (smooth) regions, one such outlined with white asterisks '*'. None of the changes found in KOs were seen in WTs. See also Figs 4D (KO) and Fig 4E (WT).

Figure S4G & H show same field. Tergazyme macerated KO femur, endosteum. An abnormal mineralising front indicating arrested or impeded collagen-fibre-bundle centred [NB NOT matrix vesicle centred!) is seen both at endosteal surfaces of the

cortex and on trabeculae: this is indicative of osteomalacias in general. Focus in Suppl Fig 4G is on trabeculum in foreground and in Fig S4H is on endosteum in background.

Suppl Figure S6C. A Tergazyme and H2O2 macerated KO tibia was embedded in PMMA, the block surface polished and stained with ammonium triiodide solution. Methacrylate has filled the blood vessel canal spaces, including those within the abnormal osteoid patches (arrows), This proves that the maceration procedure did successfully removed cell remnants from within the blood vessel canal spaces.

Figure S6D. Tergazyme and H2O2 macerated KO tibia embedded in PMMA in the fused growth plate region, showing unfused calcospherites within the calcified cartilage (Cs), which is normal, and the unfused mineralised regions within the osteoid (os), which is an abnormal phenomenon (osteomalacia).

Figure S7. Sequence of XMT slices, every tenth slice = every 50m horizontally, every 250m vertically, showing distribution of osteoid patched within cortex from KO femur. Original slice numbers outside field at edges.